POAC'25
St. John's, Newfoundland and Labrador, Canada

Proceedings of the 28th International Conference on Port and Ocean Engineering under Arctic Conditions
Jul 13-17, 2025
St. John's, Newfoundland and Labrador
Canada

Methods of laboratory investigations of wave drift of model icebergs

Aleksey Marchenko[1], Atle Jensen[2]
[1]The University Centre in Svalbard, Longyearbyen, Norway
[2]University of Oslo, Oslo, Norway

ABSTRACT

An experiment was conducted at the University Centre in Svalbard to study the drift of model icebergs in an acrylic wave flume. A model scale of 1:400 was applied on both icebergs and waves. Iceberg models of cylindrical shape (floaters) were made from paraffin. The diameters and heights of the floaters were smaller 7 cm and 6 cm, respectively. All models had stable buoyancy with vertical axis in calm water. A plunger-type wave maker generated periodic waves with a frequencies less than 4 Hz in the tank. The video recordings were used to reconstruct the movements of the floater's centers of gravity. The video recordings were processed in Wolfram Mathematica software and subjected to pixel analysis. A fiber optic strain sensor (FBG sensor) was used to measure the force applied to the floaters by waves. It was found that the mean drift speed of floaters is several times higher than the Stokes drift speed at the water surface. The amplitude of floaters movement in the vertical direction was similar the wave amplitude. The pitch oscillations of the floaters occurred around some constant non-zero pitch, which was absent in calm water. The mean value of the force applied to the floater turned out to be close was found close to the wave drift force acting on a fixed floater with a vertical axis of the same diameter as in the experiment.

KEY WORDS: iceberg, wave, wave flume, drift, surge, heave, force, video recording, fiber optic

1 INTRODUCTION

The effect of surface waves on icebergs and floes is of interest for calculating their drift in wave conditions (Smith, 1993; Eik, 2009; Keghouche et al, 2010; Monteban, D., et al., 2020). Icebergs

movements caused by waves affect ice loads on ship and offshore structures (Lever et al, 1991; Sayed et al, 2017). Lever et al (1991) noted that wave induced motions become increasingly important in predicting ice piece velocity as the size of the ice mass decreases. Field observations and numerical simulations have confirmed the influence of waves on the drift of icebergs and floes on Spitsbergen Bank (Marchenko et al, 2020; Turnbull and Marchenko, 2022).

Laboratory studies of wave-induced motion of model icebergs were carried out by Lever et al (1988) and Eik et al (2009). Experiments of Lever et al (1988) were conducted in a wave flume of 58m length and 4.15 m width with water depth of 1.8 m. The baseline scale factor was 1:70. The sizes of the iceberg models were in the range of several tens of centimeters. Four infrared light-emitting diodes were mounted on the models, together with control electronics and small batteries. The sequential firings of the LED's were tracked by two cameras. The resulting displacement information was analyzed to reconstruct model surge, heave, sway, pitch, roll, and yaw. Of greatest interest were characteristics of surge and heave depending on the shape of icebergs and wave properties. Experiments of Eik et al (2009) were carried out in a water tank of 60 m length and 5 m width with water depth of about 1 m. A model scale of 1:150 was applied on both icebergs and waves. The sizes of the model icebergs varied in the range from 60 cm to 10 cm. The iceberg displacement along the tank was measured by a laser range meter. The main objective of the experiment was to study the iceberg drift caused by waves and to estimate the drag coefficients for the mean drift of icebergs in waves.

This paper discusses the technical aspects of measuring floaters drift in smaller scale experiments with a scaling factor of about 1:400. In such experiments, the sizes of model icebergs are on the order of several centimeters, and the length of the tank can reach several meters. Organizing laboratory experiments on this scale is much cheaper. Surface waves with a length of 15-30 cm are described by standard dispersion equations, and the effects of surface tension are negligible and can be ignored. Installing sensors on model icebergs is problematic due to their small size. The water pressure forces acting on the floaters are also very small. In this paper, we describe methods for measuring the wave motion of a floater and the force of water on a floater in small scale experiments. The second section of the paper describes small-scale experiments conducted in the wave flume of the University Centre in Svalbard (UNIS). The third section of the paper discusses a method for processing video recordings of floater drift to reconstruct its motion. The use of fiber optic sensors to measure wave drift force on a floater is discussed in the fourth section of the paper. The main results of the study are formulated in the conclusions.

2 ORGANIZING OF EXPERIMENT

The experiment was organized in a wave flume at UNIS (Fig. 1). The acrylic wave flume was 3.5 m long, 50 cm high and 30 cm wide. The depth of water in the flume was 30 cm. A plunger-type wavemaker generated waves with a frequency of less than 4 Hz. The wave amplitude in the flume was determined by the frequency. In the experiment we investigated the drift of floaters made of paraffin. The density of paraffin was 800 kg/m^3. The floaters were cylindrical in shape, less than 7 cm in diameter and less than 6 cm in height. All floaters had stable buoyancy with a vertical axis in calm water. The floaters were covered with a thin dark blue plastic film to avoid the effect of light reflection on the video images of the floaters. In this paper, we present experimental results obtained with a floater of 67 mm diameter and 57 mm height.

To monitor the motion of the floaters, we installed a video camera on the side of the flume and recorded all experiments through the side wall of the acrylic flume at the water level. Figure 2 shows an example video frame. To calculate the length and amplitude of the waves, vertical and

horizontal length scales glued to the wall of the flume were used. The floater diameter was used as a length scale to calculate the metric characteristics of its motion. To reconstruct the movement of floaters at a distance of 20 cm, only video recording analysis was used.

Figure 1. Flume with wave maker at UNIS.

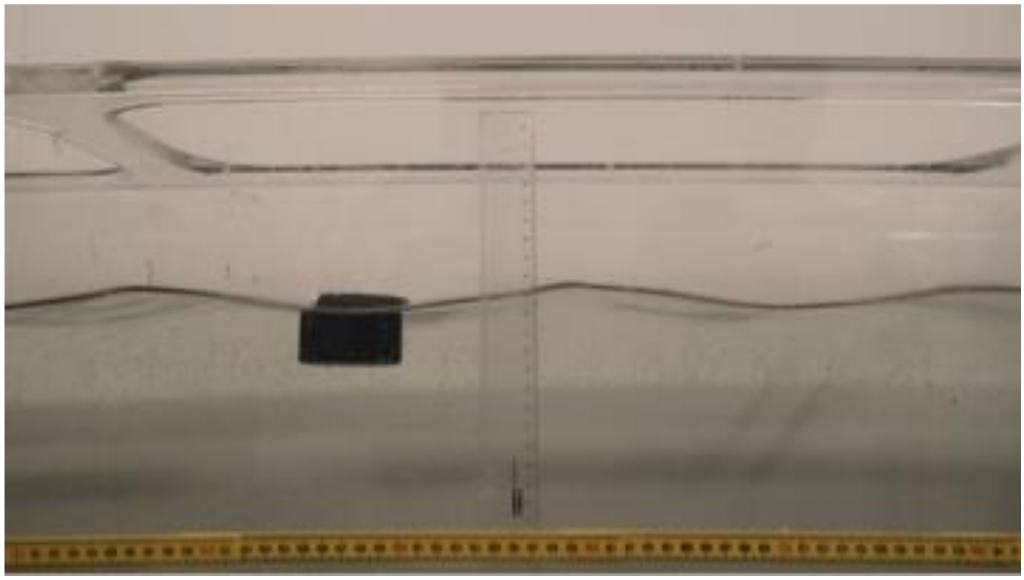

Figure 2. An example of a video frame showing the cylindrical floater drifting under the action of a periodic wave of 24 cm in length.

Figure 3a shows schematics for measuring of wave drift force on a ship in the Maruo (1960) model tests. This method was modified due to the small forces applied to the floaters in our tests (Fig. 3b). The force was measured using a calibrated Fiber Bragg Grating (FBG) strain sensor extended across the wave flume and mounted on a heavy frame that had no contact with the flume (Fig. 4). The FBG system used was designed by Advance Optic Solutions GmbH (Germany, https://www.aos-fiber.com/). The fiber with FBG sensor was connected to a floater by a thin thread passing a bearing at water level and thin metal rod at the top of the flume as it is shown in Fig. 3b. It was important that the thread was in the air, and possible contacts of the thread with water were minimized.

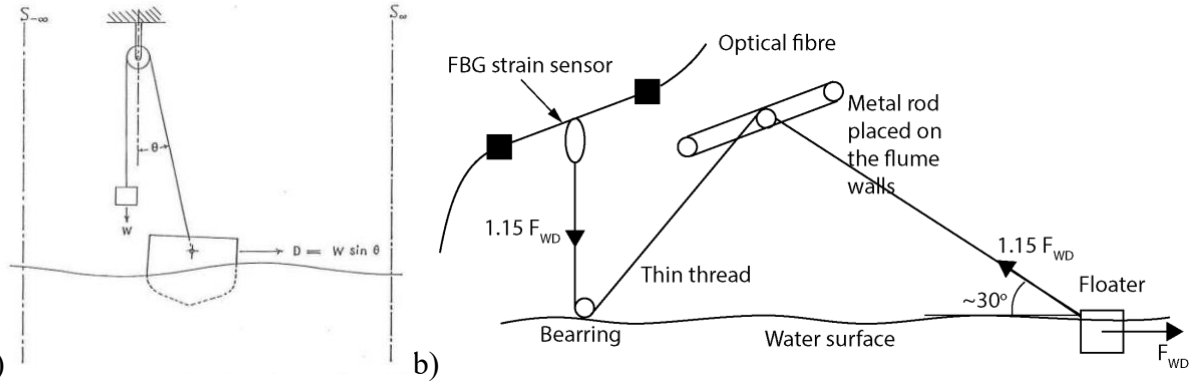

Figure 3. Schematics of measurement of drift force from Maruo (1960) (a) and used in the described experiment (b).

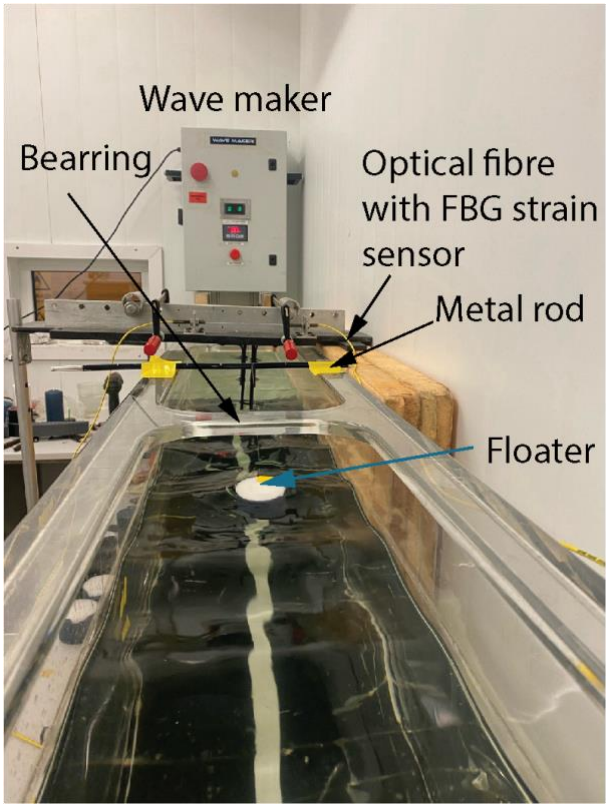

Figure 4. Photograph of the experiment in UNIS laboratory

FBG sensor measured the peak wavelength of the light reflected by the Bragg grating burned inside the fiber. FBG strain sensors are designed to operate in the wavelength range from 1510 nm to 1595 nm. Changes in the wavelength are recalculated in the fiber strain (Marchenko et al, 2016). In the experiment we used FBG strain sensor with working wavelength around 1542 nm. We didn't calculate strains and used the raw sensor data to calculate the force applied to the sensor through the thread. Calibration showed that a 20 g weight affected the change in the reflected wavelength by approximately 0.1 nm. The FBG strain sensor of 1 mstrain resolution allowed us to measure very small forces.

3 PROCESSING OF VODEO RECORDINGS

Video recordings of the experiment were used to reconstruct the movement of floating disks. The recording rate has b set at 50 frames per second. The analysis was performed in Mathematica Wolfram software and included the following steps.
Step 1: the Video function has been applied to download videos in the software environment.
Step 2: the VideoExtractFrames function has been applied to extract video frames corresponding to floaters movements in a 20 cm long observation area.
Step 3: the ImageCrop function was applied to each frame to produce a cropped footage that includes only the floater, water and water surface.
Step 4: the DominantColors function was applied to get the floater color.
Step 5: the ImageValuePositions function was applied to get the pixel coordinates of a floater image on the frames.
Step 6. The mean values of the coordinates of floater pixels were calculated for each cropped frame and then converted to actual coordinates $x = x(t_i)$ using the floater diameter as the length scale and the actual time t_i equal to the frame time. Finally, the actual displacement of the floater was interpolated by the functions $x = x(t)$ and $z = z(t)$ using the Interpolation function.
Step 7. The linear Fit of the series $x(t_i)$ was constructed: $\langle x \rangle = x_0 + \langle V \rangle t$ to obtain the mean drift velocity of the floater $\langle V \rangle$.
Step 8. The linear Fit of the series $z(t_i)$ was constructed: $\langle z \rangle = z_0 + \langle V_z \rangle t$ to exclude from consideration floater motion in the orthogonal to the x-axis direction caused by small tilt of video camera.
Step 9. The oscillating part of floater displacement was calculated with the formulas

$$\delta x_i = x(t_i) - \langle x \rangle, \delta z_i = z(t_i) - z_0, t = t_i, \quad (1)$$

and the series δx_i and δz_i were interpolated as functions $\delta x(t)$ and $\delta z(t)$.
Step 10. Based on the observations we assumed the oscillating surge motion of floaters is closed to sinusoidal motion with periods of waves exciting the motion. The amplitudes δx_0 and δz_0 of the oscillating surge motion of disks were estimated with the formula

$$\delta x_0 = 1.416\ \text{StandardDeviation}[\delta x_i], \delta z_0 = 1.416\ \text{StandardDeviation}[\delta z_i], \quad (2)$$

obtained for pure sinusoidal oscillations.

Next, we will illustrate an example of processing of a video recording of a floater with a diameter of 6.6 cm and a height of 5.5 cm. The floater was covered with dark blue plastic. The video recording was downloaded to Mathematica Wolfram software using the Video function.

$$\text{v1} = \text{Video}[\text{"S2560007.mp4"}]; \tag{3}$$

where S2560007.mp4 is the file name. A video frame of the recording is shown in Fig. 2. One can see that the plastic film was destroyed from the left side of the floater near its surface. The ImageCrop function was used to cut the frame edges, and the function VideoExtractFrames was used to create a set of images corresponding to the position of the floater on wave over each 1/50 of second starting at $t = 2$ s and ending at $t = 6$ s, where $t = 0$ correspond to the first frame of the video recording v1. We example two versions of the ImageCrop function given by

```
vc1 = ImageCrop[ImageCrop[v1, {2100, 800}, {Left, Bottom}], {1200, 400}, {Right,Top}];   (4a)
vec1 = VideoExtractFrames[vc1, Interval[{2, 6}]];
```

```
vc1 = ImageCrop[ImageCrop[v1, {1920, 200}], {1200, 30}, {Right, Top}];                   (4b)
vec1 = VideoExtractFrames[vc1, Interval[{2, 6}]];
```

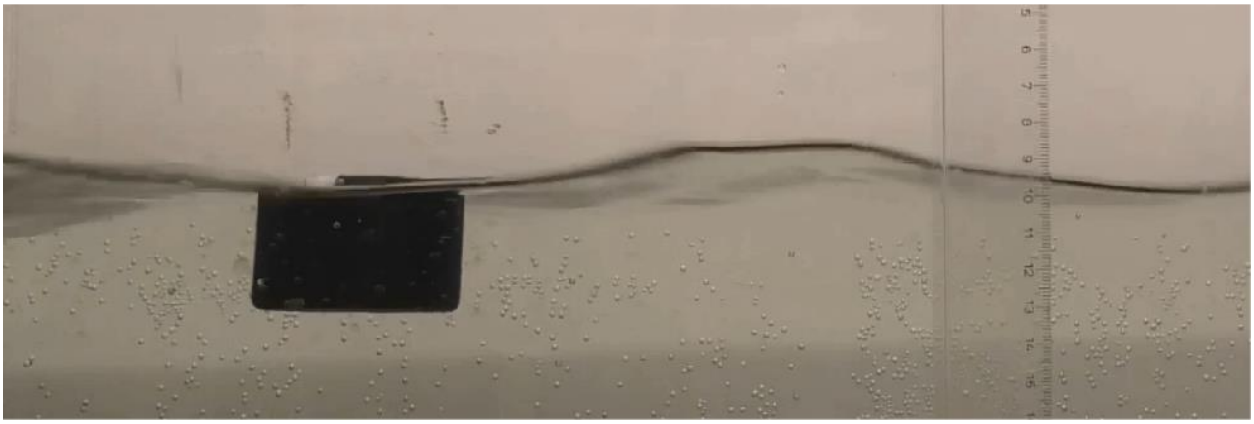

a)

b)

Figure 5. Video frame #80 extracted from the video v1 after the cutting of the frame edges using set of commands (4a) (a) and (4b) (b).

Operations (4a) and (4b) create cropped video frames similar to those shown in Fig. 5a and Fig. 5b, respectively. Further processing of video frames after performing operations (4a) allows us to reconstruct the vertical and horizontal movements of the floater's center of gravity. The influence of the water free surface distorts the analysis and leads to a decrease in the accuracy of movement recontraction. Further processing of video frames after performing operations (4b) allows us to reconstruct the horizontal movements of the floater only but leads to higher accuracy of horizontal movement recontraction. Applying the function DominantColors to video frame 1 after performing operations (4a) showed three dominant colors

$$\text{dc} = \text{DominantColors}[\text{vec1}[[1]]]; \tag{5a}$$

{■, ■, ■}

Applying the function DominantColors to video frame 1 after performing operations (4b) showed two dominant colors

$$\mathrm{dc} = \mathrm{DominantColors}\left[\mathrm{vec1}\left[[1]\right]\right]; \tag{5b}$$

{■, ■}

Color dc[[2]] corresponds to the floater. The ImageValuePositions function returns the positions of pixels with color dc[[2]] in the standard image coordinate system. The operation below constructs the list with elements including vertical and horizontal coordinates of each video frame within a distance d from dc[[2]]

$$\mathrm{ivp} = \mathrm{Table}[\mathrm{ImageValuePositions}[\mathrm{vec1}[[i]], \mathrm{dc}[[2]], d], \{i, \mathrm{Length}[\mathrm{vec1}]\}]; \tag{6}$$

The distance d was chosen visually to obtain the largest number of floater pixels while excluding pixels outside the floater. Figure 6a and 6b show pixels of two selected frames #50 and #100 constructed using operation (6) at $d = 0.09$ with the set of frames vec1 obtained by applying operations (4a). Figure 6c and 6d show pixels of two selected frames #50 and #100 constructed using operation (6) at $d = 0.09$ with the set of frames vec1 obtained by applying operations (4b).

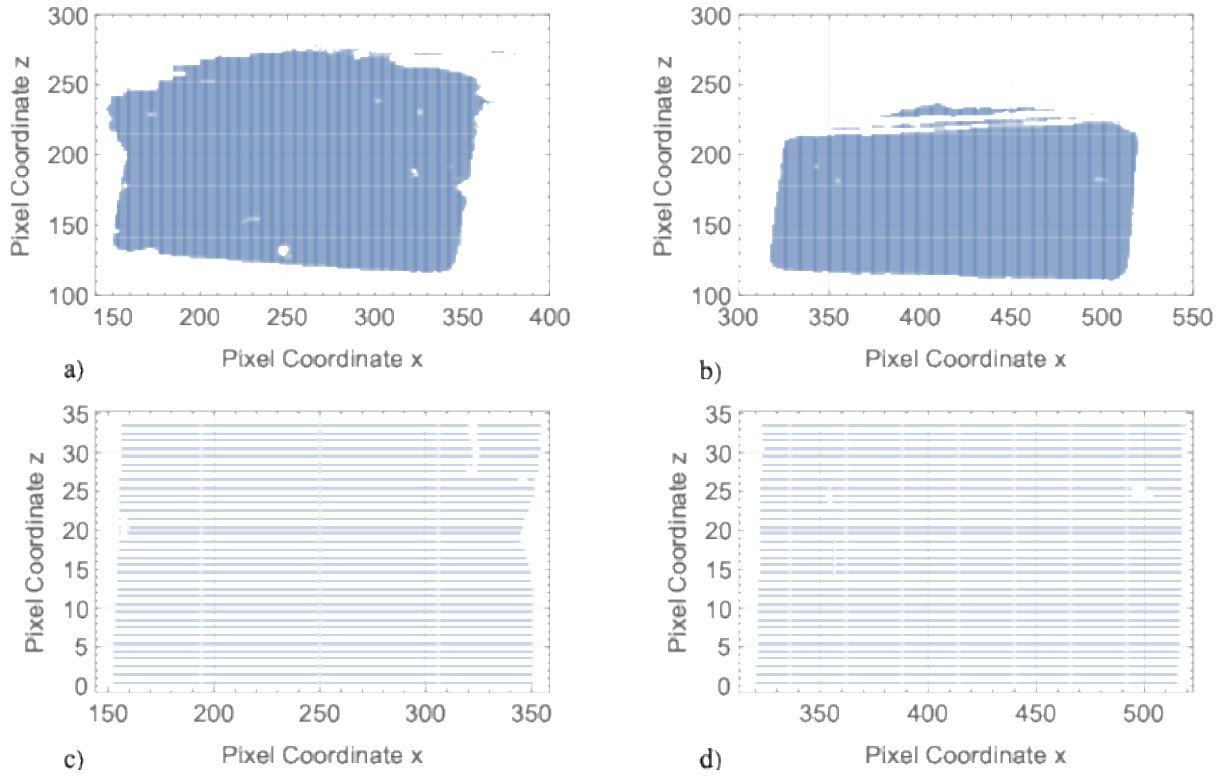

Figure 6. Pixels with color dc[[2]] in video frames #50 and #100 after the cutting of the frame edges using operations (4a) (a,b) and (4b) (c,d).

The deviation of the pixel number from the mean pixel number in the frames characterizes the accuracy of the reconstruction of disk images after the applying operations (4)-(6). The number of pixels in each frame and the mean number of pixels are calculated with the operations

$$\text{Nivp} = \text{Table}[\text{Length}[\text{ivp}[[i]]], \{i, \text{Length}[\text{ivp}]\}]; \quad (7)$$
$$\text{mivp} = \text{Mean}[\text{Nivp}];$$

Then, we calculated the ratio δ of the standard deviation of the pixel numbers in frames to the mean number of pixels using the operation

$$\delta = \text{StandardDeviation}[\text{Nivp}]/\text{mivp}; \quad (8)$$

We found that $\delta = 0.17$ for the frame list ivp obtained after the application of operations (4a), (5a), and (6), and $\delta = 0.02$ for the frame list ivp obtained after the application of operations (4b), (5b), and (6). This means that the accuracy of the reconstruction of disk images is much higher when the ImageCrop function is determined by (4b). In this case the water free surface doesn't affect the pixel analysis.
The following two operations were used to construct the mean horizontal (ddx) and vertical (ddz) positions of the floater in each video frame

$$\text{ddx} = \text{Table}\left[\text{Mean}\left[\text{ivp}[[i]]\right][[1]], \{i, \text{Length}[\text{ivp}]\}\right]; \quad (9)$$
$$\text{ddz} = \text{Table}[\text{Mean}[\text{ivp}[[i]]][[2]], \{i, \text{Length}[\text{ivp}]\}];$$

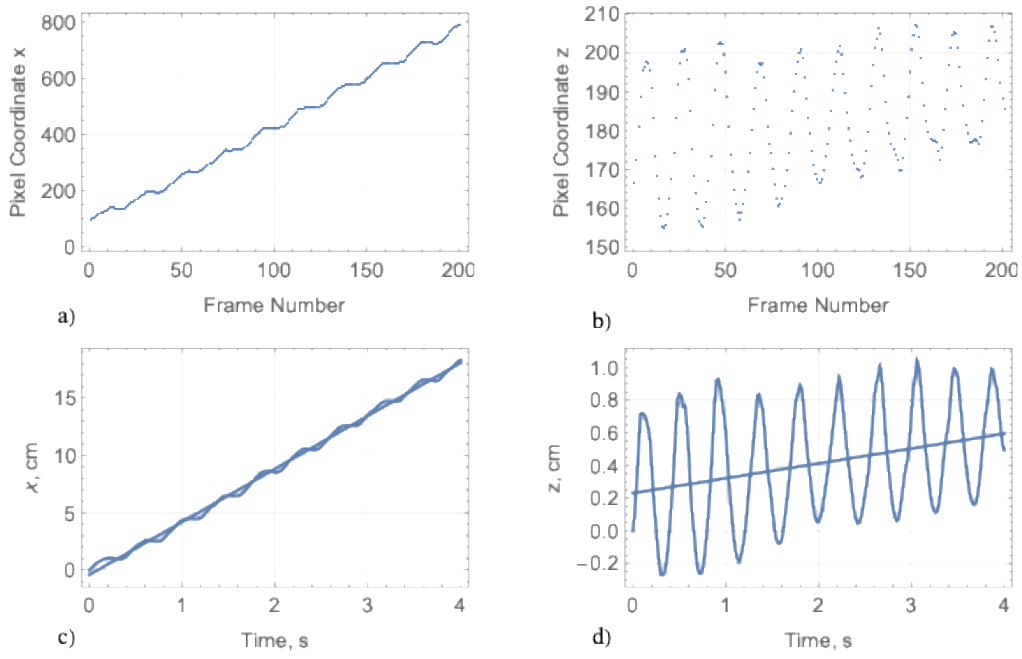

Figure 7. Horizontal (a) and vertical (b) positions of the floater in the standard image coordinate system versus the number of video frame. Horizontal (c) and vertical (d) coordinates of the gravity center of the floater in metric frame of reference versus time. Straight lines show the linear interpolations of the dependences.

We assume that the mean positions determined by formulas (9) are close to the positions of the center of gravity of the floater. Figures 7a and 7b show the mean horizonal and vertical positions of the floater versus frame number. Interestingly, the mean horizonal positions were almost identical for the vec1 lists constructed using operations (4a) and (4b). In other words, the horizontal movements of the disk images shown in Fig. 6a and 6b and Fig. 6c and 6d were almost identical. This means that the free water surface mainly influenced the reconstruction of the vertical movements of the floater.

Figures 7c and 7d show the mean horizonal and vertical coordinates of the floater in metric coordinates versus time. Straight lines in Fig. 7c and 7d show the linear interpolations of the dependences $x(t)$ and $z(t)$. The speed of wave drift in the horizontal direction equals $\langle V \rangle = 4.6$ cm/s. The mean displacement of the floater in the vertical direction is explained by the tilt of the video camera. The vertical drift was subtracted from the dependence $z(t)$ to get actual motion of the floater in the vertical direction. Figure 8a shows the floater trajectory after the subtraction of the mean drift in the vertical direction. Figure 8b shows the trajectory of the oscillatory motion of the floater, obtained after subtracting the mean drifts in the horizontal and vertical directions.

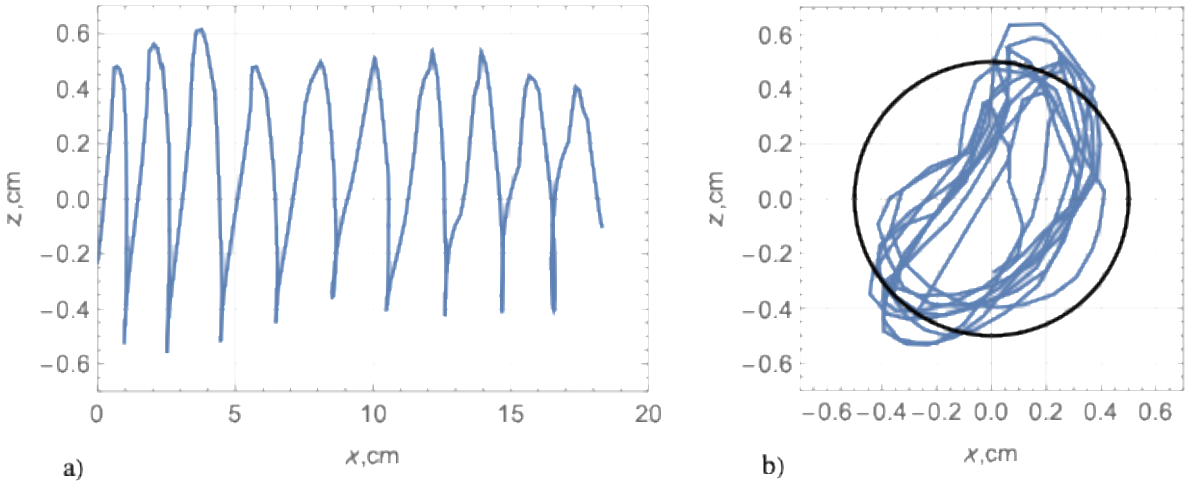

Figure 8. Trajectory of the floater's center of gravity (a). Trajectory of oscillating motion of GC of the floater (b). Solid black line shows the trajectory of water particles at the surface of deep water caused by the propagation of sinusoidal wave with the length 24 cm and the amplitude 0.5 cm.

The wavelength and wave amplitude were estimated form video recordings as 24 cm and 5 mm. Using the deep-water approximation, we calculated the wave frequency of 2.55 Hz and the Stokes drift velocity on the surface of 1 cm/s. The mean drift velocity of the floater was larger the Stokes drift velocity by 4.6 times. The trajectories of surface water particles are circles with a radius of 5 mm. Black solid line in Fig. 8b shows the trajectory of the surface water particle in comparison with the trajectory of the oscillatory motion of the floater.

The mean surge and heave amplitudes were calculated to be 34 mm and 47 mm, respectively. The heave amplitude practically coincided with the wave amplitude. The surge amplitude was smaller the wave amplitude. The inclined axis of the floater trajectory in Fig. 8b is explained by the dynamic pitch of the floater during the drift, which is absent in calm water. The pitch is also visible

in Figures 5 and 6. The dependence of pitch angle from time could be reconstructed using pixel analysis, but this operation is not described in the paper.

4 MEASUREMENT OF WAVE DRIFT FORCE

Wave drift force is the second order force applied to a submerged body by periodic wave with nonzero mean value averaged over the wave period (Faltinsen, 1990). The wave drift force on vertical cylinder in deep water is calculated by the formula

$$F_{WD} = \frac{g\rho a^2 D}{8} X_{WD}, \tag{10}$$

where a is the wave amplitude, D is the diameter of the cylinder, ρ is water density, g is the gravity acceleration. Function $X_{WD}(Dk, hk)$ depends on the dimensionless parameters Dk and hk, where k is wavelength, and h is the draft of the cylinder. Usually, $X_{WD}(Dk, hk)$ has local maximum around $Dk \approx 2$, and $X_{WD} \geq 2.5$ around the local maximum (Nossen et al, 1991). In our experiment $a = 8.5$ mm, $D = 66$ mm, and wave frequency was equal $f = 3.033$ Hz. The wavenumber calculated from the dispersion equation for deep water equals $k = 37$ m^{-1}, and $Dk \approx 2.44$. This results in an estimate of $F_{WD} \geq 0.015$ N. Measuring wave drift forces is not an easy task because they are small.

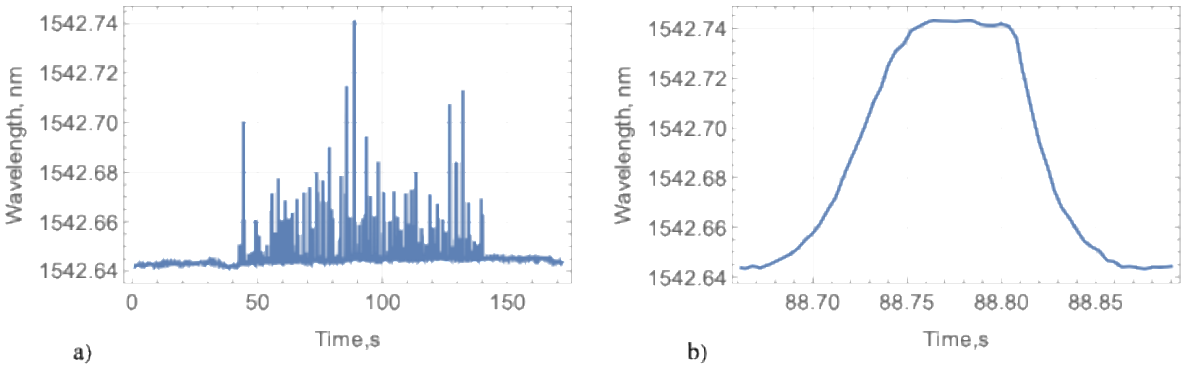

Figure 9. Wavelengths recorded by FBG strain sensors during the experiment versus time (a). Change of wavelength during strongest pulse versus time (b).

Figure 3b shows that the wave drift force F_{WD} applied to the floater in the horizontal direction results in a force $1.15F_{WD}$ applied to the fiber with FBG sensor in the downward direction. The force $1.15F_{WD}$ is proportional to the change of the wavelength measured by FBG strain sensor. It is calculated using calibration.

Figure 9a shows an example of recorded wavelengths during the experiment. One can see that changes in the wavelengths were smaller 0.1 nm. Therefore, forces applied to FBG strain sensor were smaller 0.2 N. Figure 9a shows many peaks in tension of FBG sensor which are associated with jerks of the thread. The number of threads equals $N = 86$ when time changed from 50 s to 140 s in Fig. 9a. Figure 9b shows largest peak of wavelengths versus time. The duration of the peak was 0.23 s, while the wave period was 0.33 s. Duration of all other peaks in Fig. 9a were also smaller the wave period. We assumed that the mean duration of the peaks equal $\Delta t = 0.2$ s.

The mean value of wavelength change due to jerks of the thread is calculated with the formula

$$\Delta\lambda = \int_{50s}^{140s}(WL(t) - WL0)dt\,(N\Delta t)^{-1}\,, \tag{11}$$

where $WL(t)$ is the wavelengths measured in the experiment versus time and shown in Fig. 9a, and $WL0 = 1542.6445$ nm is the background wavelength measured in the experiment before wave maker started operating. Using the experimental data, we calculated $\Delta\lambda = 0.0094$ nm. According to the calibration the force associated with this wavelength equals $F_{exp} = 0.018$ N. The horizontal projection of this force equals 0.016 N, which is very close to the wave drift force estimated using formula (8).

5 CONCLUSIONS

Processing of video recordings using Wolfram Mathematica software has shown good results in reconstructing 2D movements of cylindrical floaters in wave flume. The dark blue color of floaters helped to avoid the influence of light reflection on the pixel analysis of video frames. Following this method, we calculated the horizontal and vertical coordinates of the center of gravity of the cylindrical floaters for each video frame of the video recording with a frame rate of 50 frames per second. This allows us to plot the trajectory and velocity of the center of gravity with the same time resolution. We found that the accuracy of reconstruction of horizontal movements is higher than that of vertical movements of floaters due to the influence of the free water surface on the pixel analysis of video recordings. To avoid this effect, the method should be modified by using only submerged part of the floaters in the pixel analysis.

It was found that the mean drift speed of floaters is several times higher than the Stokes drift speed at the water surface. The amplitude of floater movements in the vertical direction was similar to the wave amplitude. We observed pitch oscillations of floaters around some constant nonzero pitch, which was absent in calm water. We believe that reconstruction of the pitch angle dependence on time is possible using the pixel analysis and Mathematica Wolfram software. The observed wave drift of the floaters can be classified as diffraction-modified Stokes drift (Xiao et al, 2024,2025).

Using of FBG strain sensor allowed us to measure the wave drift force on a cylindrical floater. The floater was connected to the fiber with FBG sensor by a thin thread so that the force applied to the floater was measured by FBG sensor. The most important points in organizing the experiment were the mounting FBG sensor on a heavy frame that had no contact with the wave flume, and the use of very thin thread connecting the floater to FBG sensor. The thread should hang in the air and have minimal contact with water. The result of the measurement was a set of force pulses with a duration shorter than the wave period. We found that the mean value of the force, averaged over all pulses, is close to the wave drift force on a fixed floater with a vertical axis and the same diameter as in the experiment.

We believe that the combination of the two methods discussed above makes it possible to calculate the drag coefficients of floaters moving under the influence of waves, depending on their shape and wave properties.

ACKNOWLEDGEMENTS

This work has been supported by the NFR sponsored project 326834: Risk of sea ice and icebergs for field development in the Southwestern Barents Sea (RareIce).

REFERENCES

Eik, K., Marchenko, A, and S. Løset, 2009. Wave drift force on icebergs-tank model tests. POAC-2009, Lulea, Sweden, June 9-12. Paper 09-86.

Eik, K., 2009. Iceberg drift modelling and validation of applied metocean hindcast data. Cold Reg. Sci. Technol. 57, 67–90.

Faltinsen, O.M., 1990. Sea Loads on Ships and Offshore Structures. Cambridge University Press, Great Britain.

Keghouche, I., Counillon, F., Bertino, L., 2010. Modeling dynamics and thermodynamics of icebergs in the Barents Sea from 1987 to 2005. J. Geoph. Res., 115, C12062.

Lever, J.H., Attwood, D., Sen, D., 1988. Factors affecting the prediction of wave-induced iceberg motion. Cold Reg. Sci. Tech., 15, 177-190.

Lever, J.H., Klein, K., Mitchell, D., Diemand, D., 1991. Wave-induced iceberg motion. Cold Reg. Sci. Tech., 20, 11-23.

Maruo, H. 1960 Wave resistance of a ship in regular head sea. Bulletin of the Faculty of Engineering, Yokohama National University, vol. 9.

Marchenko, A., Lishman, B, Wrangborg, D., Thiel. T., 2016. Thermal expansion measurements in fresh and saline ice using fibre optic strain gauges and multi-point temperature sensors based on Bragg gratings. Hindawi Publishing Corporation, Journal of Sensors, Vol. 2016, ID 5678193.

Marchenko, A., Zenkin, A., Marchenko, N., Paynter, C., Whitchelo, Y., Ellevold, T. J., Jensen, A., 2020. Monitoring of 3D motion of drifting iceberg with an ice tracker equipped with accelerometers. Proceedings of the IAHR International Symposium on ice.

Monteban, D., Lubbad, R., Samardzija, I., Loset, S., 2020. Enhanced iceberg drift modelling in the Barents Sea with estimates of the release rates and size characteristics at the major glacial sources using Sentinel-1 and Sentinel-2. Cold Reg. Sci. Tech., 175, 103084.

Nossen, J., Grue, J., Palm, E., 1991. Wave forces on three-dimensional floating bodies with small forward speed. J. Fluid Mech., Vol. 227, 135-160.

Sayeed, T., Colbourne, B., Quinton, B., Molyneux, D., Peng, H., Spencer, D., 2017. A review of iceberg and bergy bit hydrodynamic interaction with offshore structures. Cold Reg. Sci. Tech., 135, 34-50.

Smith, S.D., 1993. Hindcasting iceberg drift using current profiles and winds. Cold Reg. Sci. Tech., 22, 33-45.

Turnbull, I., Marchenko, A., 2022. Deformation of an ice pack influenced by waves and topographic enhancement of tidal motion near Hopen Island in the Barents Sea. CRST, 194, 103463.

Xiao, Q., Calvert, R., Yan, S.Q., Adcock, T.A.A., van der Bremer, T.S. ,2024 Surface gravity wave-induced drift of floating objects in the diffraction regime. J. Fluid Mech. 980, A27.

Xiao, Q., McAllister, M.L., Adcock, T.A.A., van der Bremer, T.S., 2025. J. Fluid Mech, 10(8), A18.